

Laser Plasma Instability Experiments with KrF Lasers

J. L. Weaver^a, J. Oh^b, B. Afeyan^c, L. Phillips^d, J. Seely^e, U. Feldman^f, C. Brown^e, M. Karasik^a, V. Serlin^a, Y. Aglitskiy^g, A. N. Mostovych^h, G. Hollandⁱ, S. Obenschain^a, L-Y. Chan^a, D. Kehne^a, R. H. Lehmberg^b, A. J. Schmitt^a, D. Colombant^a, A. Velikovich^a

Abstract

Deleterious effects of laser-plasma instability (LPI) may limit the maximum laser irradiation that can be used for inertial confinement fusion. The short wavelength (248 nm), large bandwidth, and very uniform illumination available with krypton-fluoride (KrF) lasers should increase the maximum usable intensity by suppressing LPI. The concomitant increase in ablation pressure would allow implosion of low aspect ratio pellets to ignition with substantial gain (>20) at much reduced laser energy. The proposed KrF laser based Fusion Test Facility (FTF) would exploit this strategy to achieve significant fusion power (150 MW) with a rep-rate system that has a per pulse laser energy well below 1 megajoule. Measurements of LPI using the Nike KrF laser are presented at and above intensities needed for the FTF ($\sim 2 \times 10^{15}$ W/cm²). The results to date indicate that LPI is indeed suppressed. With overlapped beam intensity above the planar, single beam intensity threshold for the two-plasmon decay instability, no evidence of instability was observed via measurements of $3/2 \omega_0$ and $1/2 \omega_0$ harmonic emissions.

^a Plasma Physics Division, U. S. Naval Research Laboratory, Washington, DC 20375

^b Research Support Instruments, Inc., Lanham, MD 20706

^c Polymath Research, Inc., Pleasanton, CA 94566

^d Lab. for Comp. Physics & Fluid Dynamics, U. S. Naval Research Laboratory, Washington, DC 20375

^e Space Science Division, U. S. Naval Research Laboratory, Washington, DC 20375

^f ARTEP, Inc., Ellicott City, MD 21042

^g SAIC, Inc., McLean, VA, 22102

^h Enterprise Sciences, Inc., Silver Spring, MD 20905

ⁱ SFA, Inc., Crofton, MD 21114

I. Introduction

The Laser Fusion Program at the United States Naval Research Laboratory (NRL) is considering the Fusion Test Facility (FTF) as a major facility on the development path to power production via inertial confinement fusion (ICF).¹ The FTF is being designed to produce 150 MW of fusion power with a 500 kJ, 5 Hz rep-rate deep ultraviolet (248 nm) KrF laser system in a direct-drive configuration. A key element towards reducing the cost and complexity of the FTF is the development of advanced pellet designs that can achieve substantial gain (~20 to 60) with significantly less than a megajoule of laser energy. The NRL laser fusion program has been exploring use of higher than usual ablation pressures to drive pellets to higher implosion velocities ($V \sim 400$ km/s) with a high intensity laser pulse ($I_{\text{peak}} \sim 2 \times 10^{15}$ W/cm²). The laser intensity and resulting ablation pressure is about twice that normally used in direct-drive designs for glass lasers operating at 351 nm. The higher ablation pressure allows the use of low-aspect-ratio pellet shells that are more resistant to the effects of hydrodynamic instability during the implosion. Target designs have been developed that combine low-aspect ratio targets and advanced pulse shaping that achieve gains >50 with a 500 kJ KrF laser. The 2-D analyses indicate these designs should be subject to reduced effects of hydrodynamic instability. However, this good hydrodynamic performance depends critically on use of KrF light at 2×10^{15} W/cm² to achieve the required ablation pressure (~200 Mbar). The maximum intensity that can be employed may be determined by the onset of deleterious levels of laser plasma instability (LPI).^{2,3,4} LPI could spoil the implosion by creation of hot electrons or by reduction of the ablation pressure or symmetry. The deep ultraviolet wavelength (248 nm), broad bandwidth (1-2 THz), and beam smoothing by induced spatial incoherence (ISI) of the KrF laser could raise intensity thresholds for LPI processes to levels higher than the average laser irradiation presently envisioned for the FTF.

As an example of the implosion designs under consideration for the FTF, the pellet structure, laser pulse shape, and density plot from a FAST2D simulation^{5,6,7} for a time near ignition are shown in Fig. 1. The pulse shape includes a spike prepulse to produce a tailored adiabat⁸ as well as a structured main pulse that includes a foot pulse and a ramped increase in drive intensity. This structured pulse helps to control the shock heating of the pellet during the acceleration and compression phases as the pulse rises to the high intensities (ablation pressures) needed to attain sufficient implosion velocity for ignition and gain. The designs for the FTF also exploit the capabilities of a KrF system to reduce (or ‘zoom’) the laser spot to smaller diameters during the pulse. This feature helps maintain efficient laser-pellet coupling at the time when the greatest intensity is required. The implosion in Fig. 1 achieved a yield of 27 MJ, a gain of ~54, or 90% of 1D yield despite growth of hydrodynamic instability from outer surface roughness. Details of the ongoing development of sub-MJ implosion designs with KrF lasers are discussed in another paper.⁷

Application of high intensity laser pulses to direct and indirect drive implosions is limited by the occurrence of LPI in the underdense plasma surrounding the pellet.⁹ Deep ultraviolet (248 nm) KrF lasers will help mitigate the risk from LPI. A simple figure of merit for the onset of LPI can be taken as the point at which the velocity of electron oscillations (v_{osc}) driven by the incident laser is comparable to the electrons’ random thermal velocities (v_{therm}), or $v_{osc}^2/v_{therm}^2 \sim 1$. The scaling of v_{osc}^2 with laser wavelength and intensity as $I\lambda^2$ would indicate that a KrF laser system at 248 nm could have as much as 2x higher intensity threshold compared to a frequency-tripled Nd-glass laser operating at 351 nm. The complex and nonlinear physics of LPI, however, means that this simple notion may not be realized in practice. The net effect of laser

wavelength on LPI could be greater than or less than that predicted by the $I\lambda^2$ scaling due, in part, to differences in the plasmas produced at different wavelengths and the associated inverse-bremsstrahlung absorption. Related changes could also include higher plasma temperatures and stronger gradients in the underdense plasma.

In addition to the shorter wavelength, the KrF lasers for FTF will incorporate superior beam smoothing by induced spatial incoherence (ISI) and large bandwidth capability ($\Delta\nu \sim 1-2$ THz) which will also impact the amount of LPI. The first experiments with the ISI smoothing were conducted at NRL using ISI on Pharos,¹⁰ a Nd:glass laser. In these experiments, ISI smoothing was implemented with an echelon based technique¹¹ for intensities ranging from 10^{13} to 10^{14} W/cm². The inclusion of ISI smoothing demonstrated a strong reduction in stimulated Brillouin and stimulated Raman backscatter for 1.054 μm light.^{12,13} For 0.527 μm operation, experiments with varied laser bandwidths ($\delta\omega/\omega \sim 0.0002\%$ to 0.3%) showed that the combination of broad bandwidth ISI smoothing and shorter laser wavelength caused the hard x-ray emission from LPI-generated hot electrons to fall by two orders of magnitude.^{14,15} ISI smoothing suppresses filamentation of the laser beam which is probably one of the main mechanisms for the suppression of other types of LPI.^{16,17}

There is not sufficient theoretical or experimental knowledge to provide precise predictions for LPI effects expected for the FTF. If the limits set by LPI on peak intensity are lower than used in the designs, then the viable alternatives would likely require higher laser energy to obtain similar gain. On the other hand if peak intensities above 2×10^{15} W/cm² are tolerable with KrF lasers, the available design options would be increased, e.g. allow still higher ablation pressure and even lower aspect ratio pellet designs. The need to develop an experimental database of LPI

with KrF lasers has led us to initiate an experimental effort to understand the LPI risk and identify the highest acceptable laser intensity. The target physics program at NRL has routinely used the Nike laser facility to provide experimental data on hydrodynamic instability and means for its mitigation. These experiments use large focal spots ($D=0.75$ mm) and 4 ns full-width at half maximum (FWHM) pulses with $I \leq 10^{14}$ W/cm². Here we report on the first Nike experiments at intensities above 10^{15} W/cm² to explore possible laser-plasma instabilities. This paper will discuss recent extension of Nike operation to such high intensities and its applications to experiments for LPI. The instability thought to be the largest threat to direct drive is the two-plasmon decay instability which typically produces odd half harmonic emission as a by product. In earlier work, ISI with 1 THz bandwidth was observed to help suppress emission due to two-plasmon decay. Observations of odd half integer harmonics of the laser frequency will be presented that show no evidence for this instability despite having an overlapped intensity that is above the calculated threshold for a single planar beam.

II. Laser-Plasma Instabilities for FTF development

The current experiments concentrate on three of the most prominent parametric instabilities: two-plasmon decay instability ($2\omega_p$), stimulated Raman scattering (SRS), and stimulated Brillouin scattering (SBS). Each is a three-wave interaction where the incoming laser light couples to either electron plasma waves (EPW) or ion acoustic waves (IAW) and can produce a scattered electromagnetic wave (EMW) or plasma waves:

Two – plasmon decay : laser \rightarrow EPW + EPW
 Stimulated Raman scattering : laser \rightarrow EMW + EPW
 Stimulated Brillouin scattering : laser \rightarrow EMW + IAW

$2\omega_p$ and SRS are of particular interest because subsequent conversion of energy from the electron plasma waves to energetic streaming electrons^{18,19,20} could result in significant heating of the compressed fuel, which can reduce gain and prevent ignition. Stimulated Brillouin scattering is expected to only occur at low levels with KrF due to the short laser wavelength and the inclusion of beam smoothing by ISI. SBS would primarily result in a slightly reduced ablation pressure, an effect that might be compensated by using slightly greater driver energy. The current experimental effort includes diagnostics to study scattering of the incident laser light via all three of these instabilities.

The above priorities for the experiments have been guided by analysis of conditions predicted for the FTF by hydrodynamic simulations. The analysis is based on plane wave average intensity thresholds for the scattering of 248 nm light traversing an inhomogeneous plasma^{21,22,23}

$$I_{2\omega_p} > 0.216 T_e / L_n \quad (1)$$

$$I_{SBS} > 0.68 T_e \left/ \left[\frac{n}{n_c} L_v \right] \right. \quad (2)$$

$$I_{SRS} > 16 / L_n \quad (3)$$

where the intensities are in units of 10^{15} W/cm², L_n ($=n/(dn/dx)$) is the density scale length in units of 100 μ m, L_v ($=v/(dv/dx)$) is the velocity scale length in units of 100 μ m, T_e is the electron temperature in keV, and n_c is the critical density for 248 nm light ($\sim 1.8 \times 10^{22}$ cm⁻³) and n is the electron density (cm⁻³) at a given position in the coronal plasma. The SRS formula refers to convective growth at densities below $\frac{1}{4} n_c$ and the SBS formula describes convective growth for subcritical densities.

Figure 2 shows the results of applying the above formulae to a simulation of an FTF implosion with the average intensity of the laser spot ($\langle I_{\text{laser}} \rangle$): $2\omega_p$ is driven over threshold early in the pulse and is $\sim 6\times$ over threshold during the peak intensity, SRS remains below threshold throughout the implosion, and SBS approaches threshold near the time of the peak intensity (~ 9 ns for the implosion analyzed here). Additionally, a graphic representation of the threshold formulae for $2\omega_p$ and convective SRS is shown in Fig. 3 where the threshold intensities are plotted as a function of density scale length. For a given set of plasma conditions, intensities above the plotted line indicate operation above the given instability threshold. The empty diamond symbols plotted on Fig. 3 show the conditions at the $\frac{1}{4} n_c$ surface throughout the 2D simulation of the implosion shown in Fig. 1. At each point, the electron temperature is indicated by the color of symbol and the associated scale is included on the figure. Stimulated Raman scattering is seen to occur at very high laser intensities on this plot. The $2\omega_p$ threshold is much lower than the SRS threshold, although the temperature dependence adds an additional complication. The main conclusion from these considerations is that the FTF designs have limited LPI risk except for $2\omega_p$.

Estimates based single planar beam thresholds include neither the effects of finite angles between overlapped beams nor the effects of the rapidly varying speckle resulting from the individual beam's spatial and temporal incoherence. In particular, transient localized regions of higher intensities (up to $\sim 5\times\langle I_{\text{laser}} \rangle$) in the focal spot are expected despite the time averaged beam smoothing. For beam smoothing by ISI, these speckles change in time and space and the resulting complexity for the physics of LPI is one of the motivations for developing an LPI program at NRL. Reliable predictive models for the energy distribution of hot electrons created by a given level of LPI are not yet available. The ISI-related experiments with Pharos

demonstrated that $2\omega_p$ -related emission required much higher bandwidth (\sim THz) to reduce its amplitude than was required to reduce SRS.¹⁴

III. Nike laser facility

The Nike KrF laser was designed primarily to explore ICF relevant hydrodynamics using a planar geometry. The system successfully demonstrated the operation of a high energy (2-3 kJ) KrF laser system with beam smoothing by echelon-free induced spatial incoherence (ISI).^{24,25} This beam smoothing technique produces beams with time-averaged spatial nonuniformities of 1% or less, see Fig. 4. When all the beams from the angularly multiplexed KrF amplifiers are overlapped on target, their speckle patterns are statistically independent, thus further reducing the laser nonuniformity to even lower levels (0.3% or better for the \sim 40 beams typically used with a 4 ns averaging time). However, the growth times for parametric instabilities can be sub-picosecond, so the instabilities may be influenced by the instantaneous speckle nonuniformities in the focal distributions. The Nike laser pulses typically have a 0.7 ps coherence time. The combination of spatial incoherence and relatively short coherence time is predicted to be more than sufficient to suppress filamentation because this process occurs on a longer hydrodynamic timescale.

The relatively long pulse lengths available from the main beam array of the Nike laser (\sim 4 ns) provide a highly uniform ablation pressure to drive hydrodynamic experiments. To provide target diagnosis, a twelve-element backlighter beam array was incorporated into the Nike system to irradiate an x-ray source for radiographic imaging of the main target. This technique has been extensively used in hydrodynamic studies of driven targets²⁶ but, as will be discussed in Sec. IV, we simplified the diagnostic to image the focal spot at the main target. In the present application

(see Fig. 5), x-rays emitted at the target are imaged by a spherically bent x-ray crystal. The narrow-band Bragg reflectivity and optical figure of the crystal generate a monochromatic and magnified 2D image of the self emission from the target. Either 2D time-integrated or 1D time-resolved spatial information was obtained with a streak camera.

We can use Fig. 3 to compare typical Nike operation relative to the threshold for $2\omega_p$. A pair of points in Fig. 3 have been plotted (purple circles joined by solid line) to show the range of intensity and density scale length for planar plasmas typically created with the main beams of the Nike laser. The color of these points represents the low temperatures at the $\frac{1}{4} n_c$ surface predicted by 2D simulations of a CH target driven by a 4 ns long square pulse at $I \sim 10^{14}$ W/cm². (The assigned color is consistent with the temperature scale included on Fig. 3). These points demonstrate that, under usual Nike operations, the plasma conditions are relevant only for an early portion of the FTF's laser pulse and span a limited region of parameter space for LPI.

IV. High Intensity Nike Operation

The main requirement to explore the relevant LPI parameter space on the Nike laser is achieving higher operating intensity. During 2006, higher intensities ($I \sim 2 \times 10^{15}$ W/cm²) have been produced using smaller focal spots and higher power pulses. The effort to date has used the backlighter beam array. The backlighter array was constructed with f/20 lenses which can provide tighter focal spots than the f/40 main beam lenses. (The Nike optical system was designed to add controlled spatial incoherence and thereby eliminate nonuniformities in the time-averaged focal spot due to phase aberrations; the main beams typically operate at 60-100 times the diffraction limit (XDL)). Another advantage with this approach is that the spot size and pulse

shape of the backlighter array are controlled independently from the main beams, so experimentation to generate high intensities can occur with little effect on the main laser system.

Initial studies to achieve tighter focal spots were conducted at low energy and were diagnosed using an adaptation of the technique originally developed to determine the beam profile of the main beams.²⁷ The oscillator and first amplifier for the backlighter beam train were used to illuminate a fluorescent glass target that was placed at the focus of the backlighter array. A magnified image of the fluorescer emission was recorded by a CCD camera to provide $\sim 3 \mu\text{m}$ on-target resolution. We do not see a significant difference in the focal distribution with the amplifiers on, provided the laser gas in the large amplifiers has sufficient time to cool between shots (presently ~ 30 minutes). The spot size on target was set by the choice of apertures used as part of the ISI smoothing in the initial stages of the laser chain. The measurements (see Fig. 6) show that Nike can achieve beam spots with 75-125 μm full width at half maximum (FWHM), or about $\sim 15\text{XDL}$ for the backlighter lens array. Along with the use of shorter higher power backlighter pulses, as discussed below, this choice of spot size provides sufficient areal reduction to achieve the desired intensity increase in the current LPI experiments. Although further reductions in spot size are possible, they have not been pursued due to associated reduction of plasma scale lengths expected for smaller focal spots. For experiments without preformed plasma, short scale lengths would lead to higher thresholds according to the discussion in Sec. II. The low intensity measurements have also demonstrated that for the chosen spot size, the standard deviation for the relative shot-to-shot pointing error between pairs of beams is $\sim 30 \mu\text{m}$. This result demonstrates that adequate overlap for high intensity operation can be achieved for the smaller focal spots.

The second element that was required for high intensity operation was the generation and amplification of short backlighter pulses in the laser chain. A critical element for this is a high-speed, high-voltage pulser used to drive the Pockels cells in the Nike front end. Figure 7 compares the 5 ns pulse typically used to backlight driven targets to the ~ 0.4 ns short pulse used for the LPI experiments. The laser emission seen after the spike is due to electrical ringing of the Pockels cell driver and can be reduced in the future with further refinements. The peak power of the spike is $\sim 4\times$ higher than that of the 5 ns pulse. This difference occurs because the KrF laser behaves as a storage medium on sub-nanosecond time scales. Although the spike's ~ 0.4 ns width is an order of magnitude shorter than the 5 ns pulse, its energy is within a factor $(0.4 \text{ ns} \times 23)/(5 \text{ ns} \times 6) \sim 0.3$ of the 36 J in the longer pulse. This result combined with the ability to create smaller focal spots has enabled high intensity operation.

To verify operation at full power with the combination of spike pulse and small spots, pinhole cameras and the x-ray crystal imaging system were used to record the self emission from a variety of targets, Fig. 5. Figure 8 shows a sample set of images. The pinhole camera images ($h\nu > \sim 1 \text{ keV}$) and time-integrated streak camera results with the monochromatic x-ray crystal imager ($h\nu \sim 1.86 \text{ keV}$) provide consistent results. Time-resolved streak images provide time histories that faithfully reproduce the laser pulse. From these studies and the energy and pulse shape laser diagnostics we can estimate the intensity for each beam. For the data shown in Fig. 8, a single beam average intensity of $2 \times 10^{14} \text{ W/cm}^2$ has been achieved. When 10-12 backlighter beams are overlapped on target, we can expect to achieve an average intensity of over $2 \times 10^{15} \text{ W/cm}^2$. This new capability greatly enhances the options for experiments to explore LPI at 248 nm as shown in the Fig. 3 (blue line and circles).

V. LPI Experiments at the Nike Laser Facility

Two basic schemes are considered for experiments: we can attempt to study instabilities at shorter scale lengths with targets driven only by a single set of beams (backlighter or main beams) or we can attempt to control plasma conditions with use of the main beams for plasma creation/heating prior to irradiation with the high intensity pulse from the backlighters. For this paper, we will present sample results with both types of experiments as development is ongoing. As shown in Fig. 5, the main beam array and the backlighter beam array are separated by 135° . When only one set of beams are used, the target normal was aligned along the centerline of the chosen beam array. Two different geometries for using both beam arrays simultaneously are discussed at the end of this section.

We have conducted FAST2D hydrodynamic simulations to estimate the plasma conditions expected for various experimental conditions. Two-dimensional hydrodynamic simulations were preferred over 1D simulations because they provide more accurate scale lengths for the small focal spots used in the experiments. Two representative laser pulse shapes were simulated for three different target materials: a 10^{14} W/cm² Nike pulse (~40 overlap beams, 750 μ m FWHM spot, 4 ns) is compared to a short pulse, small-spot pulse at 2×10^{15} W/cm² (10 overlap beams, 145 μ m FWHM spot, 0.4 ns) on a polystyrene (CH) target, a boron nitride (BN) target, and a cryogenic DT target. Figure 9 shows the density plots for the two pulse shapes for the CH target. Although the experiment will be done with cryogenic D₂, for the purposes of this paper this slight material difference should represent a minor perturbation to the hydrodynamic evolution of the target.

The estimated plasma conditions, see Table I, can be used to evaluate the occurrence of $2\omega_p$ according to Eqn. 1. For the 4 ns square pulse on CH, the low incident intensity and the significant reduction of this intensity at the $\frac{1}{4} n_c$ surface predict that the $2\omega_p$ process will not take place. For the spike case, the high incident intensity and reduced absorption up to $\frac{1}{4} n_c$ allow all three targets to be above threshold. The density scale length is reduced in these cases - only slightly increasing the threshold. This analysis assumes that $2\omega_p$ will react to the average intensity of the overlapped beams in the same manner as for a single beam of the same intensity.

Scattered radiation diagnostics for $2\omega_p$ have focused on measuring the odd half-integer harmonics of the drive laser, namely $\frac{1}{2}\omega_0$ at 496 nm and $\frac{3}{2}\omega_0$ at 165 nm. Emissions at $\frac{1}{2}\omega_0$ and $\frac{3}{2}\omega_0$ have been routinely observed in LPI experiments on the Omega laser facility at the LLE of the University of Rochester.^{28,29} Early work at the Omega 24 beam facility with a 351 nm laser at similar intensities to this experiment demonstrated that the $\frac{1}{2} \omega_0$ and $\frac{3}{2} \omega_0$ signatures could be observed for plastic (CH) spheres with and without Ti or Ni coatings (50-400 μm diameter) and at intensities as low as $\sim 1\text{-}2 \times 10^{14} \text{ W/cm}^2$ without beam smoothing. Two broad peaks shifted to either side of the exact odd half harmonic frequency were observed for both odd half harmonics. An additional central peak with less broadening was seen over a narrow central cone of the backscatter collection optics for the $\frac{1}{2} \omega_0$ emission. This feature was interpreted as a result of a hybrid $2\omega_p$ -Raman instability occurring near the $\frac{1}{4} n_c$ surface.^{23,30} Later work at the Omega laser revisited³¹ $2\omega_p$ and SRS thresholds at laser intensities up to $\sim 10^{15} \text{ W/cm}^2$ with the application of beam smoothing with distributed phase plates (DPP) and smoothing by spectral dispersion (SSD). With an incident intensity of $\sim 10^{15} \text{ W/cm}^2$ and FM bandwidth of $\Delta\lambda/\lambda \sim 0.03\%$ for SSD

smoothing, the $2\omega_p$ detection threshold was seen to increase by a factor ~ 2 while the SRS signal was observed to decrease by three orders of magnitude.

In this section, data will be shown from time-integrated and time-resolved spectrometers that cover the spectral range from 150 nm to 600 nm. These spectrometers were placed at various locations around the target chamber and were limited to relatively large observation angles outside the cone angle of the beam arrays. A time-integrated vacuum ultraviolet (VUV) spectrometer³² ($150 \text{ nm} < \lambda < 250 \text{ nm}$) was placed at an angle $\sim 30^\circ$ to the target normal. A fiber optic collector for time-integrated visible light spectrometers (i.e. $\sim 240 \text{ nm} < \lambda < 800 \text{ nm}$) was placed at $40\text{-}50^\circ$ to the target normal. Finally, a time-resolved visible light spectrometer ($240 \text{ nm} < \lambda < 525 \text{ nm}$) was placed in the chamber with a line-of-sight of $\sim 15^\circ$ to the target normal. The time-resolution for this spectrometer was provided by a linear array of Si photodiodes. Each element in the array recorded the light over a relatively broad wavelength range ($\delta\lambda \sim 26 \text{ nm}$) with moderate time resolution ($\delta t \sim 0.7 \text{ ns FWHM}$). Glass filters were used with the visible light spectrometers to block the laser wavelength (248 nm) to ensure that any observed signal at $\frac{1}{2} \omega_0$ was due to LPI and not higher orders of the diffraction gratings. Lastly, for the longer wavelength light ($\lambda > 250 \text{ nm}$), collection optics are being prepared for exact backscatter through the final focusing lenses for a few beams. X-ray pinhole cameras and filtered x-ray diodes were deployed for monitoring emission in the 1-10 keV range. An array of photomultiplier/scintillator detectors is being prepared to monitor emission of hard x-rays ($100 \text{ eV} < h\nu < 100 \text{ keV}$) due to hot electrons generated by LPI.

To provide reference data, we conducted laser shots at low intensity ($I < 10^{14}$ W/cm²) for a variety of targets using Nike's main beams and a 0.750 mm focal diameter. Sample spectra are shown in Fig. 10 for BN targets and CH targets for several shots. The VUV spectrum shows the time integrated spectrum for BN from 150 nm to 250 nm. This spectrometer did not have collection optics, so, although it responds to light from the laser focal spot, it also responds to the regions around the focal spot that are heated by lateral thermal conduction. In Fig. 10, these cooler regions add spectral lines from the lower ionization stages of the target material (and surface contaminants). An expansion of the VUV spectrum around 165 nm in Fig. 10 shows the lack of $3/2\omega_0$ emission more clearly. The BN target is chosen because it lacks the spectral lines at 165 nm that were seen at all intensities for CH targets. In the expanded view, no evidence for emission at $3/2\omega_0$ is observed. Similarly, time-integrated and time-resolved visible light spectra for CH targets for two separate low intensity laser shots are shown in Fig. 10. The time-integrated data are for a main beam spot, while the time-resolved data are for a large spot, 5 ns long pulse backlighter shot. Both results demonstrate that for low intensities, no spectral signatures for LPI are evident, as expected from the threshold estimates.

Similar data were obtained for backlighter beam shots where the overlapped laser intensity is estimated to be above the single planar beam threshold for the $2\omega_p$ instability (Eqn. 1). Figure 11 presents data for two different shots where, for each target, the laser intensity was above the thresholds calculated in Section II. The first spectrum in Fig. 11a shows time integrated VUV spectrum for a small spot, spike pulse ($I \sim 1.6 \times 10^{15}$ W/cm²) on BN. If the plasma conditions are as predicted by the simulation, this target should have conditions over the threshold for $2\omega_p$. The spectrum seems to have only small changes from the low intensity data shown in Fig. 10.

Similarly, the VUV spectrum for an over-threshold shot is shown in Fig. 11a for a cryogenic D2

target irradiated at 2×10^{14} W/cm². A time resolved visible light spectrum (Fig. 11b) for $\frac{1}{2}\omega_0$ emission for CH irradiated at 2.5×10^{15} W/cm² also shows very similar results to the low intensity observations. For these data, the odd-half harmonic emission appears to be consistent with the absence of two-plasmon decay.

These results can be contrasted to recent spherical and planar experiments at the Omega laser³³ where the $\frac{3}{2}\omega_0$ emission, fractional heating by hot electrons, and hard x-ray signal were observed as a function of overlapped intensity. These signals were found to vary with the total overlap intensity rather than the individual beam intensity. The lack of $\frac{3}{2}\omega_0$ emission observed in our experiments at intensities above the single beam threshold argues against such a dependence, but additional work remains to be done. This work includes (i) an improved understanding of LPI driven with the unique properties of ISI light from the Nike laser discussed above, (ii) a complete commissioning of the LPI diagnostics under development (including an improved $\frac{3}{2}\omega_0$ spectrometer with temporal and spatial resolution and time-resolved hard x-ray detectors), and (iii) possible extension of Nike operation to even higher single-beam intensities.

Stimulated Raman scattering at densities below quarter critical density as referred to in Eqn. 3 can lead to broadband emission between ω_0 and $\frac{1}{2}\omega_0$. The results in Fig. 10b, 10c, and 11b indicate that time-resolved visible spectra in this region are unremarkable and show only small wavelength-dependent changes between low intensity and high intensity shots. Figure 11c compares spectra from a standard Nike intensity ($I < 10^{14}$ W/cm²) to one from a high intensity shot ($I > 2 \times 10^{15}$ W/cm²). These spectra are taken from the data in Fig. 10c and 11b, at 3 ns and 1.35 ns, respectively. The cut-off around 300 nm in Fig. 10c and 11b is due to the attenuation of glass filter used in the experiments to prevent unwanted laser light at 248 nm from contaminating

the data. The shape of the normalized spectra in Fig. 11c (with the points below ~ 300 nm removed) are similar despite the difference in incident laser intensity and appear to represent gray-body emission. Absolute calibration of the photodiodes is in progress to allow analysis of signal levels. As for the odd half-harmonics discussed above for $2\omega_p$, the lack of signature emission between ω_0 and $\frac{1}{2}\omega_0$ is interpreted as the absence of stimulated Raman scattering.

LPI experiments have begun with the high intensity backlighter beams incident on preformed plasmas, see Fig. 12. The main beams at low intensity are used as heating beams to create a moderate temperature, long scale length plasma. After a 2-5 ns delay, the small spot, short pulse backlighter beams are fired into this plasma to generate LPI. Two configurations have been tried: one configuration rotates the target so both the heater and spike beams can strike the same side of the target and the other configuration has the main beams strike the side opposite from the backlighter beams. This second configuration used heater beams to ‘explode’ the target from one side and heat it to at least moderate temperature before the probe pulse is fired from the opposite side. One potential advantage to this latter approach is the simplicity that the target normal (hence the axial density gradient) is oriented along the direction of laser propagation. This geometry makes interpretation of the probe/plasma wave coupling for LPI modeling less complicated. At this time, standard thickness targets (~ 30 - 40 μm) were used for the experiments and planar 1D simulations indicate that it is likely only low temperatures (~ 100 eV) were achieved. Although no signature of odd half-harmonic emission was observed for the shots, at such low temperatures, it is expected that collisional absorption of the probe pulse will cause the light to be below threshold at the $\frac{1}{4}n_c$ surface. Future experiments are planned with much thinner targets (1-5 μm thick CH) that should create plasmas heated to much higher temperatures.

A sample of the combined front side data for a BN target from the time-integrated VUV and visible light spectrometers is shown in Fig. 12. For these data, the main beams had an intensity of $8 \times 10^{13} \text{ W/cm}^2$ and the probe beam had an intensity of $6 \times 10^{14} \text{ W/cm}^2$. The VUV spectrum shows little change from the low intensity shots, while the visible spectrum also appears similar to the low intensity shots except for an apparent dip around 450 nm and a peak at 550 nm. This spectrum is not currently understood and will be further investigated with upcoming shots. These heater/probe beam experiments are a start to the development of a suitable platform for the ongoing LPI program at NRL.

VI. Summary

A promising new parameter regime for achieving substantial gain with sub-MJ laser facilities has led to an examination of laser-plasma instabilities driven by high intensity KrF lasers. The Nike laser at NRL is being used to study LPI with the recent extension to operation around $I \sim 2 \times 10^{15} \text{ W/cm}^2$, a regime relevant to the FTF. Although Nike will not be able to reproduce the full set of conditions for the desired implosions, these experiments will develop a basis for future studies with higher energy facilities as they become available. For one of the most significant LPI processes, the two-plasmon decay instability, the VUV and visible spectra presented in this paper show no $\frac{1}{2} \omega_0$ or $\frac{3}{2} \omega_0$ emissions from these processes for conditions where the overlapped beam intensity was greater than the single beam inhomogeneous threshold for growth. Ongoing work includes improved control of the plasma conditions and more thorough diagnosis of the LPI interactions.

VII. Acknowledgements

The authors would like to thank NRL personnel for their dedicated support for these experiments. The expert operation of the Nike laser facility was provided by Steve Terrel, Zeb Smyth, Laodice Granger, Bruce Jenkins, Steve Krafsig, Nicholas Nocerino, Jonathan Piccotta, and Rachel Dicht. Drew Fielding and Joseph Kelleher provided invaluable design and fabrication support. We would also like to acknowledge valuable discussions with John Gardner, especially in support of the FAST2D simulations used in this paper. This work was supported by U.S. Department of Energy

Figure Captions

Figure 1 (color):

Sample pellet and pulse shape for an implosion for the Fusion Test Facility (FTF) are shown.

The cross section of the pellet shown in a) is spherically imploded by deep ultraviolet (248 nm)

KrF laser with the pulse shape shown in b). Two-dimensional simulations, part c), indicate that ignition and gain (~ 54) can be achieved with this 500 kJ system.

Figure 2:

From the 2D hydrocode simulations of implosions on FTF, analyses for intensity thresholds of two-plasmon decay, stimulated Raman scattering, and stimulated Brillouin scattering show that $2\omega_p$ appears to be the most significant LPI process. SBS can appear at low levels near the peak of the pulse, while SRS is below threshold throughout the shot.

Figure 3 (color):

Graph showing relationship between density scale length ($L_n \sim (n/(dn/dx))$) and threshold intensity for a single planar beam in an inhomogeneous plasma. The plotted lines show the thresholds for $2\omega_p$ (dotted lines) and convective SRS (dashed line). The three lines for the $2\omega_p$ instability span an approximate range of expected temperatures for conditions of interest to FTF. The plotted points show the regions for expected conditions at the $1/4 n_c$ surface for an implosion at the FTF (diamond symbols), low intensity Nike operation (purple circles and line), and high intensity Nike operation (blue circles and line). The colors for all of the symbols (diamonds and circles) are assigned according to electron temperatures estimated from simulations (color table in upper right). The separation of the conditions for the FTF and those for the Nike laser underscore the need for experiments with higher energy lasers to create relevant plasma conditions.

Figure 4:

Beam smoothing by induced spatial incoherence has been implemented on the Nike laser at NRL. For averaging times (1-4 ns) much larger than the coherence time (~ 0.7 ps), the RMS nonuniformity has been shown to be $< 1\%$. When 40 statistically independent beams are overlapped, the non-uniformity is reduced to $\sim 0.2\%$. The inset image shows a time-integrated measurement of the beam profile at the position of the main target.

Figure 5 (color):

At the Nike laser, there are two beam arrays available for experiments with a 135° separation as measured relative to the target chamber center. For high intensity operation, the current work has utilized the backlighter beams. An x-ray optical system based on a spherically bent quartz crystal has been used to make monochromatic images of self emission from targets placed at the center of the target chamber. Time-integrated 2D images and time-resolved 1D images were recorded with a streak camera.

Figure 6:

Images of three different Nike backlighter beams taken at low energy show the smaller focal spots achieved.

Figure 7:

These plots compare a 5 ns long backlighter pulse shape to the 0.4 ns long pulse shape used for high intensity operation. The propagation of short pulses has resulted in $\sim 4\times$ increase in power.

Figure 8 (color):

X-ray images of a) time-integrated pinhole image of x-rays from the focal spot for 9 overlapped beams on Au (0.4 ns pulse), b) time-integrated image of 10 overlapped 5 ns long beams striking a Au target, and c) time-resolved image of a single beam on a Si target. For b) and c), the self-emission was imaged using the spherically bent x-ray crystal imager. Time and space line-outs from the streaked image show that the small spot and short pulse length are maintained for full

power operation of the Nike laser. The average intensity of this single beam shot is estimate to be $I \sim 2 \times 10^{14} \text{ W/cm}^2$, so for 10-12 overlapped beams, average intensities greater than $2 \times 10^{15} \text{ W/cm}^2$ can be created.

Figure 9 (color):

Density plots from FAST2D hydrocode results CH targets irradiated by (a) a low intensity pulse ($I=10^{14} \text{ W/cm}^2$) and (b) a high intensity pulse ($I=2 \times 10^{15} \text{ W/cm}^2$). The data from these simulations are shown in Table I and can be used to estimate the expected threshold intensities according to Eq. 1.

Figure 10:

Sample spectra from low intensity Nike shots on CH and BN. The time integrated VUV result (a) for BN shows a number of lines from low charge states of the target material (and contaminants) but no signature of the $2\omega_p$ instability even under an expanded scale. Time-integrated (b) and time-resolved visible light spectra (c) at roughly the same intensity also show no signatures for the $1/2 \omega_0$ emission.

Figure 11:

Sample spectra from high intensity Nike shows for BN and cryogenic D2 (a), and CH (b). In all three cases, the laser intensity of the overlapped beams was over the single beam threshold for inhomogeneous plasmas. No signatures of the $1/2 \omega_0$ or $3/2 \omega_0$ emission are seen in these spectra. In part (c), comparison of normalized spectral lineouts from 10c and 11b for 3 ns and 1.35 ns, respectively, also show that the shape of the broadband spectra between $1/2 \omega_0$ and ω_0 changed little for the different laser intensities.

Figure 12:

Sample spectra from combined main beam/backlighter beam shots. The main beams arrived ~ 4 ns before the backlighter beams to generate a plasma to support the laser-plasma instability. The

VUV and visible spectra again show no signatures of odd half harmonic emission.

Table I: Plasma conditions at the $\frac{1}{4} n_c$ surface are taken from 2D simulations for two separate pulse shapes on three target materials.

Parameter	CH		BN		DT	
(at $Ne_{crit}/4$):	Nike ^a	Gaussian ^b	Nike ^a	Gaussian ^b	Nike ^a	Gaussian ^b
L_n (μm)	172	78.4	151.3	64.4	257	84.7
T_e (eV)	899	2321	966	2455	755	1673
I_{laser} ($10^{15} W/cm^2$)	0.029	1.70	0.025	1.58	0.061	1.78
$I_{laser}/I_{2\omega p}$ thresh	0.26	2.66	0.18	1.92	0.96	4.17

^a at 2 ns

^b at peak power

References:^j

-
- ¹ S. P. Obenschain, D. G. Colombant, A. J. Schmitt, J. D. Sethian, M. W. McGeoch, *Physics of Plasmas*, **12**, 056320 (2006).
- ² S. E. Bodner, D. G. Colombant, J. H. Gardner, R. H. Lehmberg, S. P. Obenschain, L. Phillips, A. J. Schmitt, J. D. Sethian, R. K. McCrory, W. Seka, C. Verdon, J. P. Knauer, B. B. Afeyan, H. T. Powell, *Physics of Plasmas*, **5**, 5, 1901 (1998).
- ³ W. L. Kruer, *Physics of Plasmas*, **7**, 6 (2000).
- ⁴ E. M. Campbell, *Physics of Fluids B*, **4**, 11 (1992).
- ⁵ A. J. Schmitt, D. G. Colombant, A. Velikovich, S. Zalesak, J. H. Gardner, D. E. Fyfe, N. Metzler, *Physics of Plasmas*, **11**, 5, 2716 (2004).
- ⁶ S. Zalesak, A. Schmitt, A. Velikovich, J. Gardner, *Physics of Plasmas*, **12**, 056311 (2005).
- ⁷ D. Colombant, A. Schmitt, S. Obenschain, S. Zalesak, A. Velikovich, J. Bates, submitted to *Physics of Plasmas*.
- ⁸ R. Betti, K. Anderson, J. Knauer, T. J. B. Collins, R. L. McCrory, R. W. McKenty, S. Skupsky, *Physics of Plasmas*, **12**, 4, 042703, (2005).
- ⁹ W. L. Kruer, *The Physics of Laser Plasma Interactions* (Addison-Wesley, Boulder, 1988).
- ¹⁰ J. M. McMahon, R. P. Burns, T. H. DeRieux, R. A. Hunsicker, R. H. Lehmberg, *IEEE Journal of Quantum Electronics* **QE-17** (9), 1629-1638 (1981).
- ¹¹ R. H. Lehmberg, S. P. Obenschain, *Optics Communications*, **46** (1), 27-32, (1983).
- ¹² S. P. Obenschain, C. J. Pawley, A. N. Mostovych, J. A. Stamper, J. H. Gardner, A. J. Schmitt, S. E. Bodner, *Physical Review Letters*, **62**, 7, 768 (1989).
- ¹³ A. N. Mostovych, S. P. Obenschain, J. H. Gardner, J. Grun, K. J. Kearney, C. K. Manka, E. A. McLean, C. J. Pawley, *Physical Review Letters*, **59**, 11 1193 (1987).
-

-
- ¹⁴ S. P. Obenschain, J. Grun, M. J. Herbst, K. J. Kearney, C. K. Manka, E. A. McLean, A. N. Mostovych, J. A. Stamper, R. R. Whitlock, S. E. Bodner, J. H. Gardner, R. H. Lehmberg, *Physical Review Letters*, **56**, 26, 2807 (1986).
- ¹⁵ T. A. Peyser, C. K. Manka, S. P. Obenschain, K. J. Kearney, *Physics of Fluids B*, **3**, 6 1479 (1991).
- ¹⁶ A. J. Schmitt, *Physics of Fluids*, **31**, 10 3079 (1988).
- ¹⁷ A. J. Schmitt, B. B. Afeyan, *Physics of Plasmas*, **5**, 2, 503 (1998).
- ¹⁸ B. Yaakobi, C. Stoeckl, W. Seka, J. A. Delettretz, T. C. Sangster, D. D. Meyerhofer, *Physics of Plasmas*, **12**, 6, 062703, 2005.
- ¹⁹ D. W. Phillion, E. M. Campbell, K. G. Estabrook, G. E. Phillips, F. Ze, *Physical Review Letters*, **49**, 19, 1405 (1982).
- ²⁰ N. A. Ebrahim, H. A. Baldis, C. Joshi, R. Benesch, *Physical Review Letters*, **45**, 14, 1179 (1980).
- ²¹ M. N. Rosenbluth, *Physical Review Letters*, **29**, 565 (1972).
- ²² C. S. Liu, in *Advances in Plasma Physics*, edited by A. Simon and W. Thompson (Interscience, New York, 1976), Vol. 16, p. 121.
- ²³ B. B. Afeyan, *Physics of Plasmas*, **4**, 3788, 3803, 3827 and 3845 (1997).
- ²⁴ S. P. Obenschain, S. E. Bodner, D. Colombant, K. Gerber, R. H. Lehmberg, E. A. McLean, A. Mostovych, M. S. Pronko, C. J. Pawley, A. J. Schmitt, J. D. Sethian, V. Serlin, J. A. Stamper, C. A. Sullivan, J. P. Dahlburg, J. H. Gardner, L.-Y. Chan, A. V. Deniz, J. Hardgrove, T. Lehecka, M. Klapisch, *Physics of Plasmas*, **3** (5), 209-2107, part 2 (1996).
- ²⁵ R. H. Lehmberg, J. Goldhar, *Fusion Technology*, **11**, 3, 532 (1987).

-
- ²⁶ Y. Aglitskiy, T. Lehecka, A. Deniz, J. Hardgrove, J. Seely, C. Brown, U. Feldman, C. Pawley, K. Gerber, S. Obenschain, R. H. Lehmberg, E. McLean, M. Pronko, J. Sethian, J. Stamper, A. Schmitt, C. Sullivan, G. Holland, M. Laming, Review of Scientific Instruments, **68**, 806 (1997).
- ²⁷ A. V. Deniz, T. Lehecka, R. H. Lehmberg, S. P. Obenschain, Optics Communications, **147**, 4-6, 402 (1998)
- ²⁸ W. Seka, B. B. Afeyan, R. Boni, L. M. Goldman, R. W. Short, K. Tanaka, T. W. Johnston, Physics of Fluids, **28** (8), 2570 (1985).
- ²⁹ K. Tanaka, L. M. Goldman, W. Seka, M. C. Richardson, J. Soures, E. A. Williams, Physical Review Letters, **48**, 17, 1179 (1982).
- ³⁰ B. Afeyan, E. Williams, Physical Review Letters, **75**, 4218 (1995).
- ³¹ W. Seka, R. E. bahr, R. W. Short, A. Simon, R. S. Craxton, D. S. Montgomery, A. E. Rubenchik, Physics of Fluids B, **4**, 7, 2232 (1992).
- ³² J. F. Seely, U. Feldman, G. E. Holland, J. L. Weaver, A. N. Mostovych, S. P. Obenschain, A. J. Schmitt, R. H. Lehmberg, B. Kjornarattanawanich, C. A. Back, Physics of Plasmas, **12**, 062701 (2005).
- ³³ C. Stoeckl, R. E. Bahr, B. Yaakobi, W. Seka, S. P. Regan, R. S. Craxton, J. A. Delettrez, R. W. Short, J. Myatt, A. V. Maximov, Physical Review Letters, **90**, 23, 235003-1 (2003).

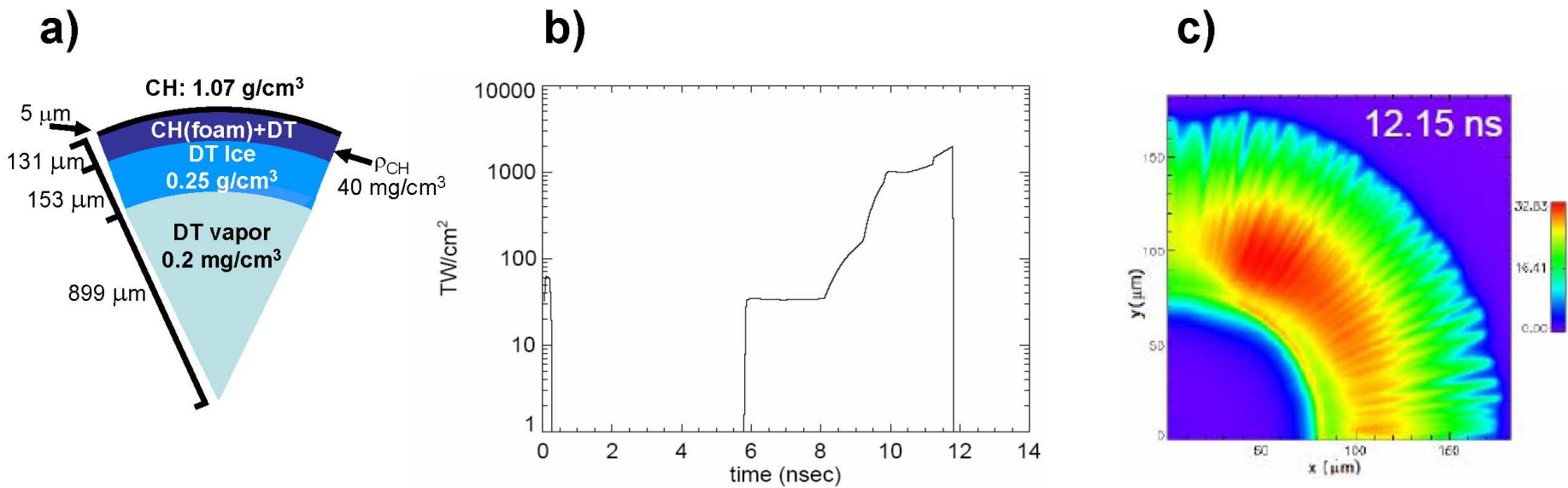


Fig. 1

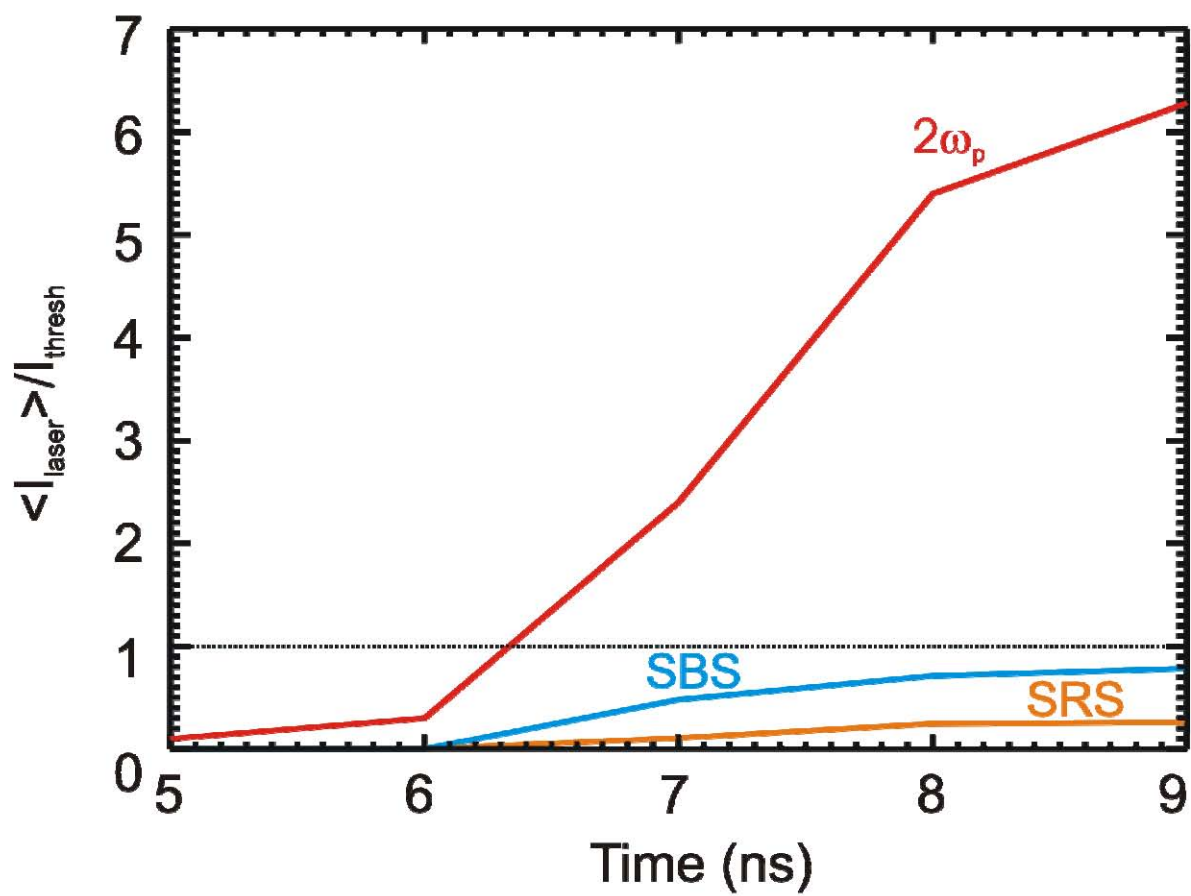


Fig. 2

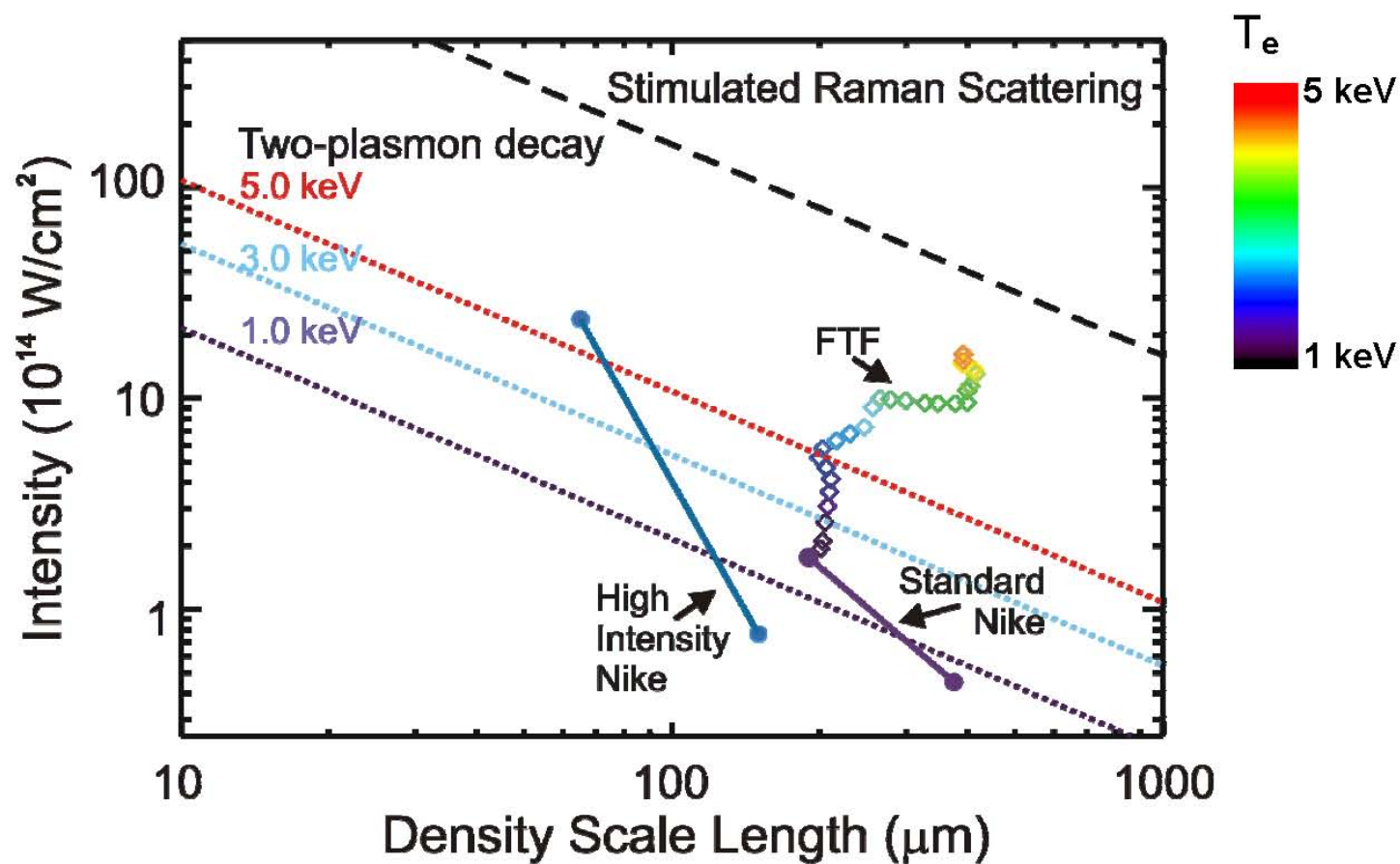


Fig. 3

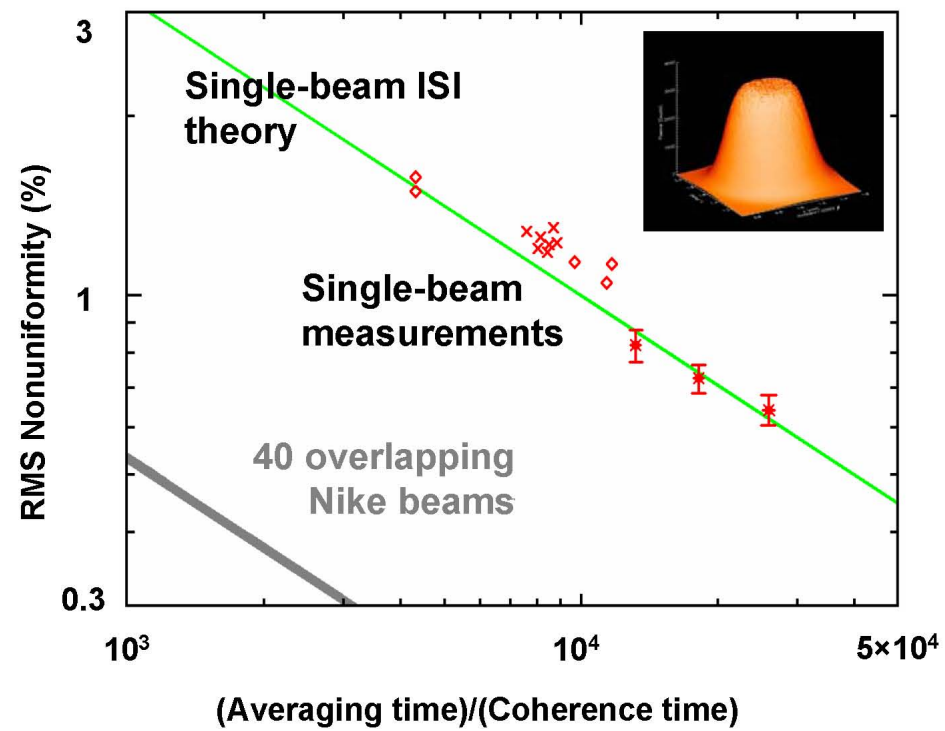


Fig. 4

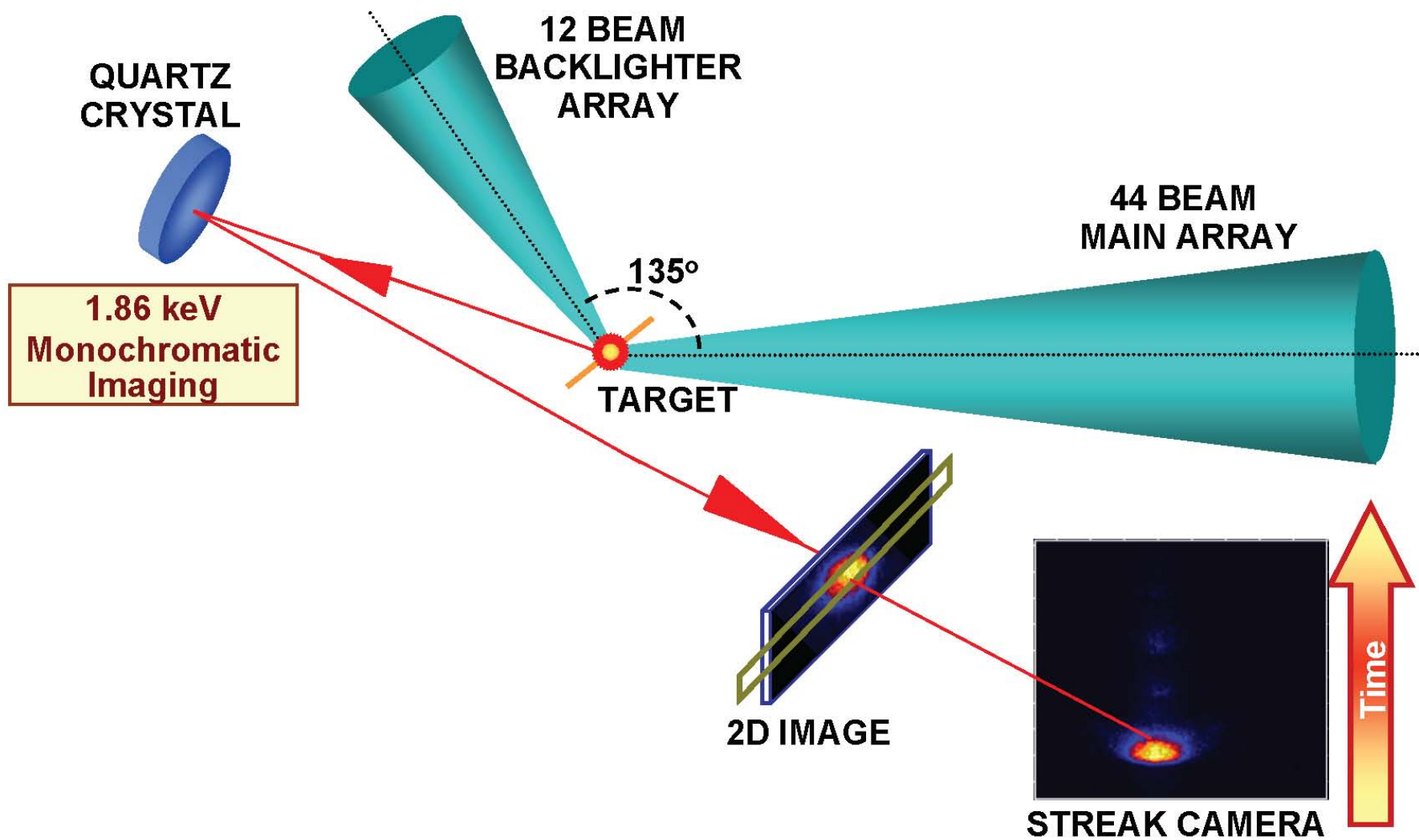
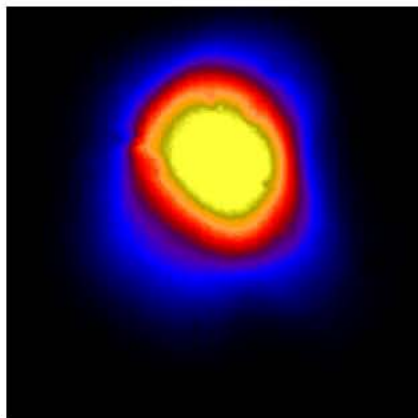
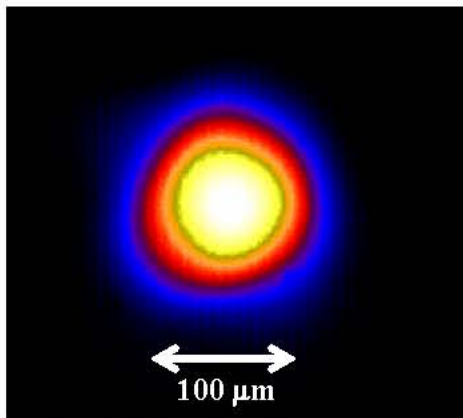


Fig. 5

Beam 1



Beam 4



Beam 32

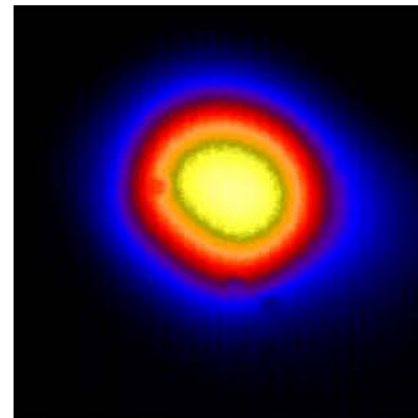


Fig. 6

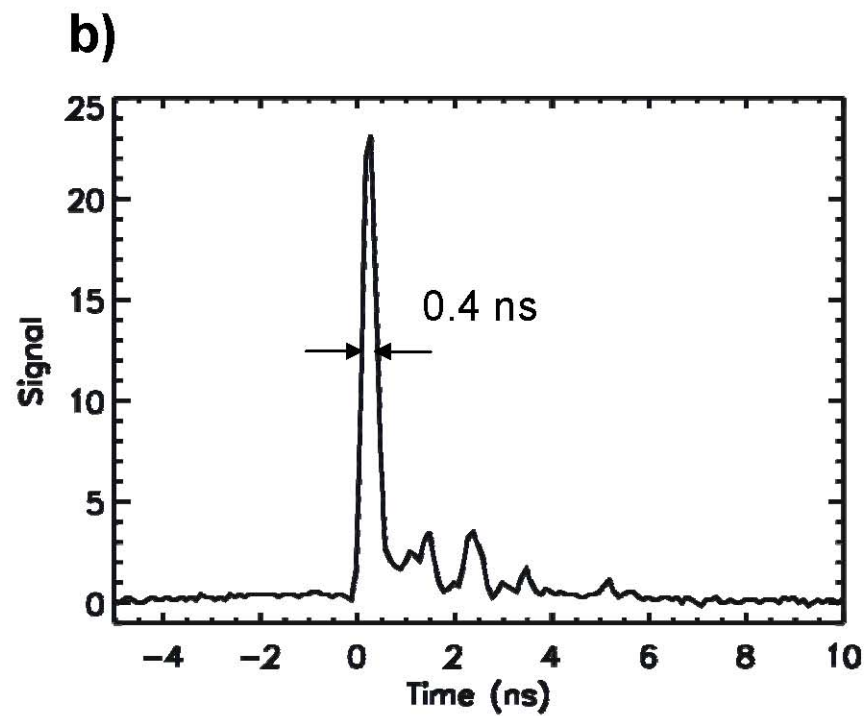
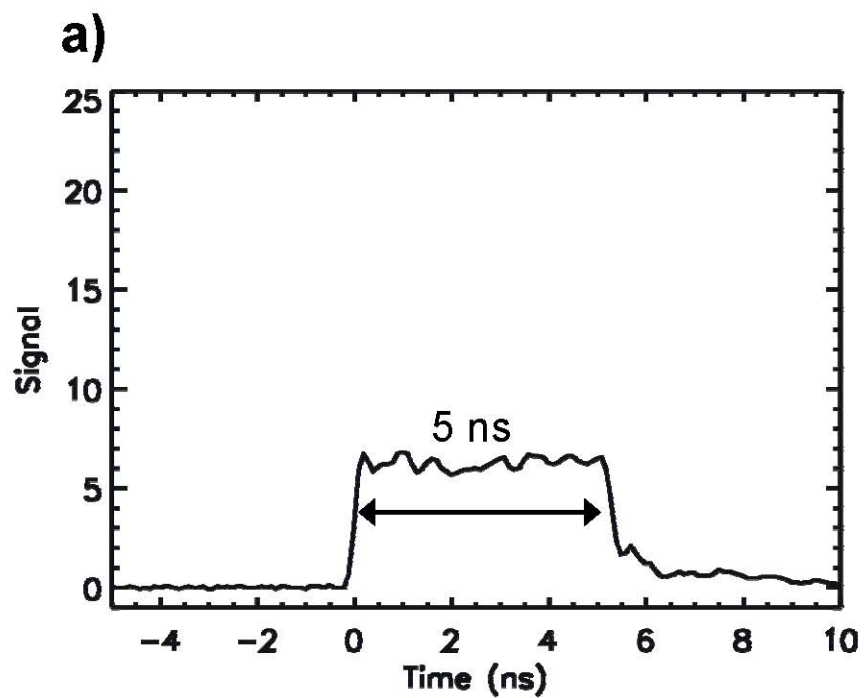


Fig. 7

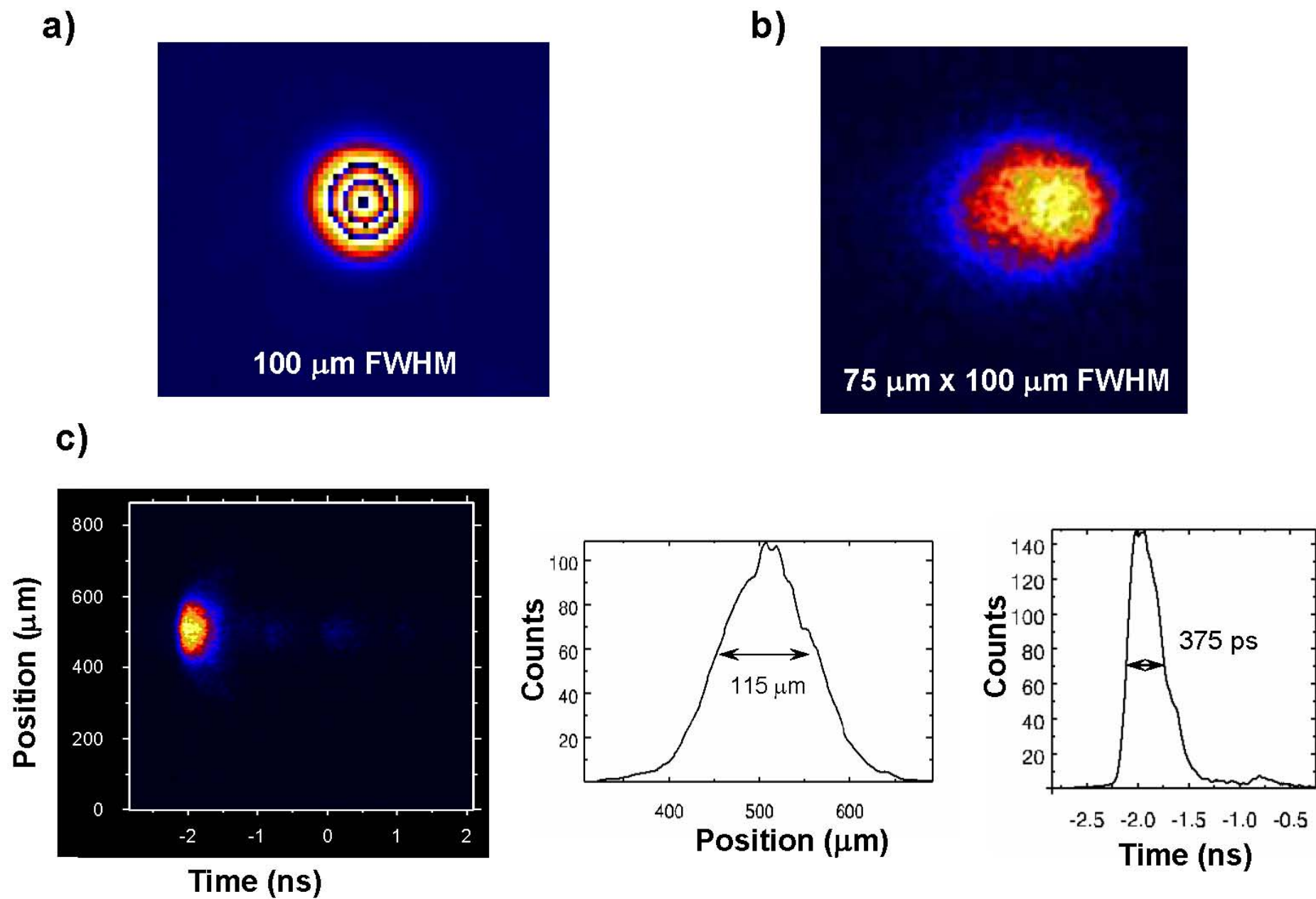
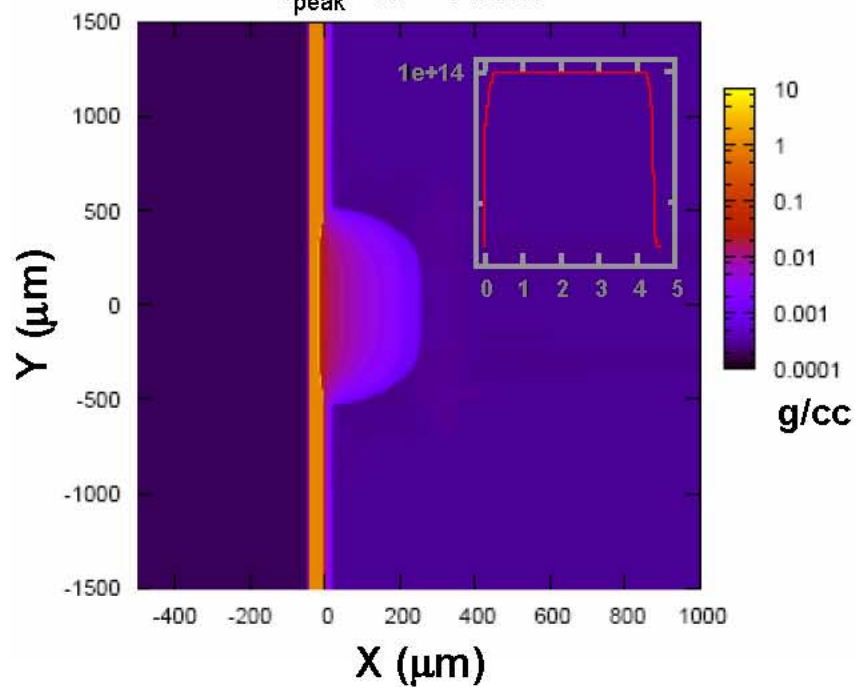


Fig. 8

a)Square pulse: 4 ns, 750 μm spot

$$I_{\text{peak}} = 10^{14} \text{ W/cm}^2$$

**b)**Gaussian pulse: 0.4 ns, 145 μm spot

$$I_{\text{peak}} = 2 \times 10^{15} \text{ W/cm}^2$$

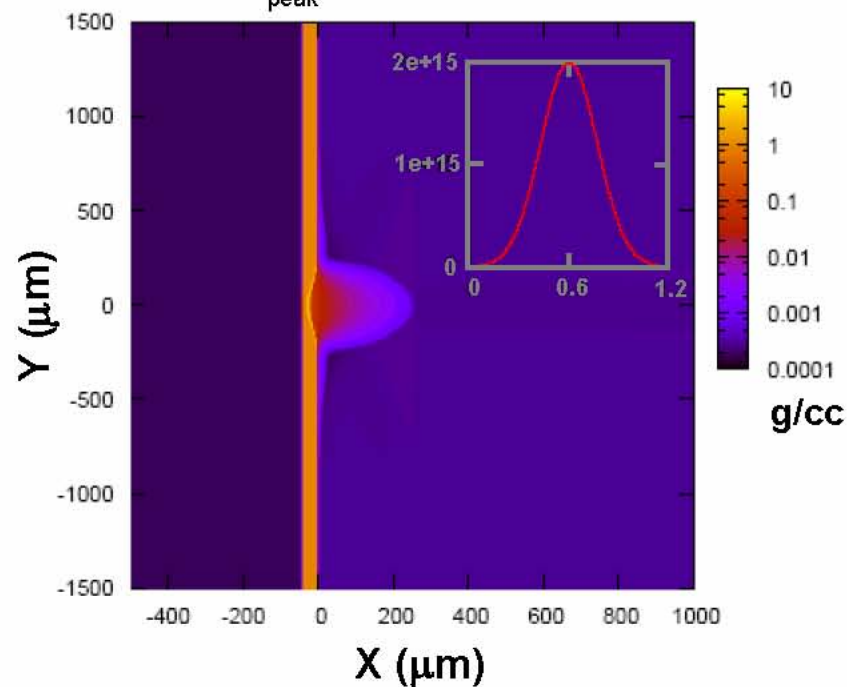
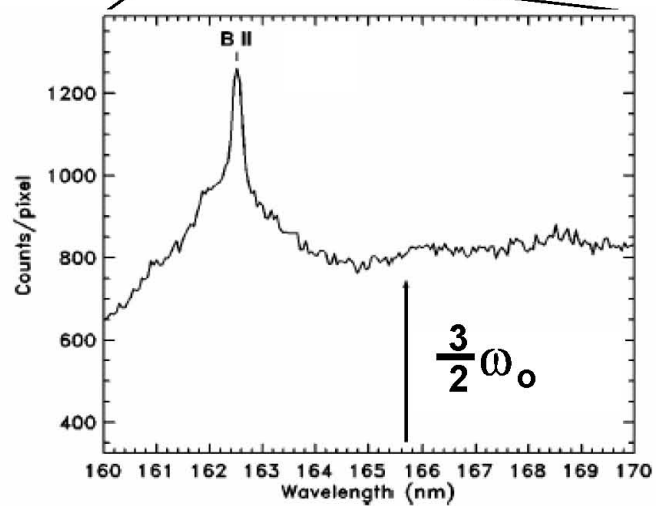
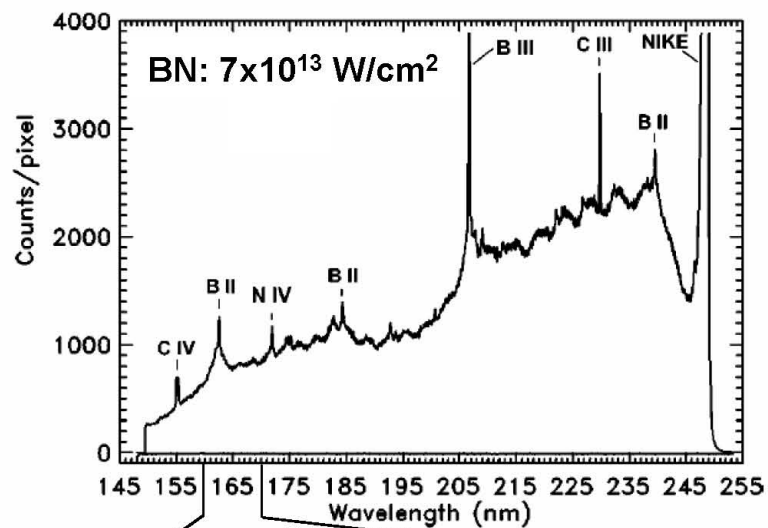
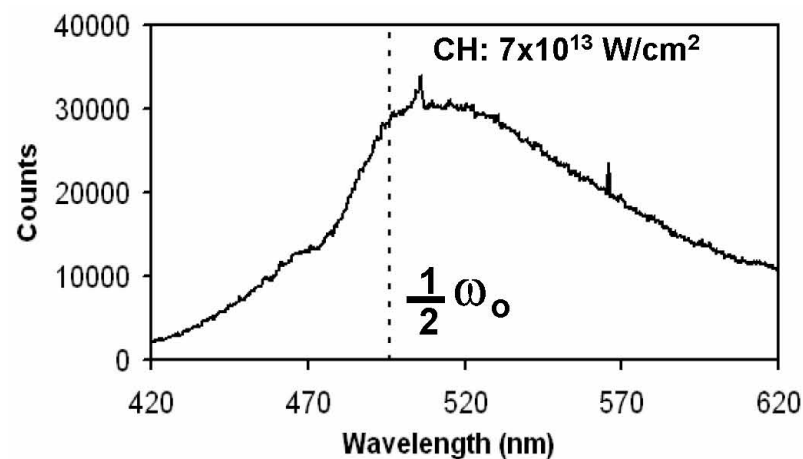


Fig. 9

a)



b)



c)

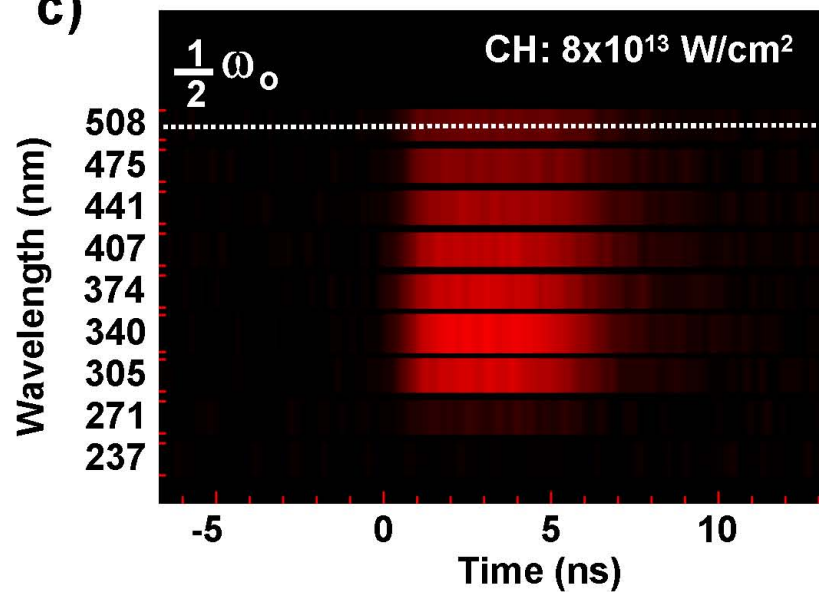
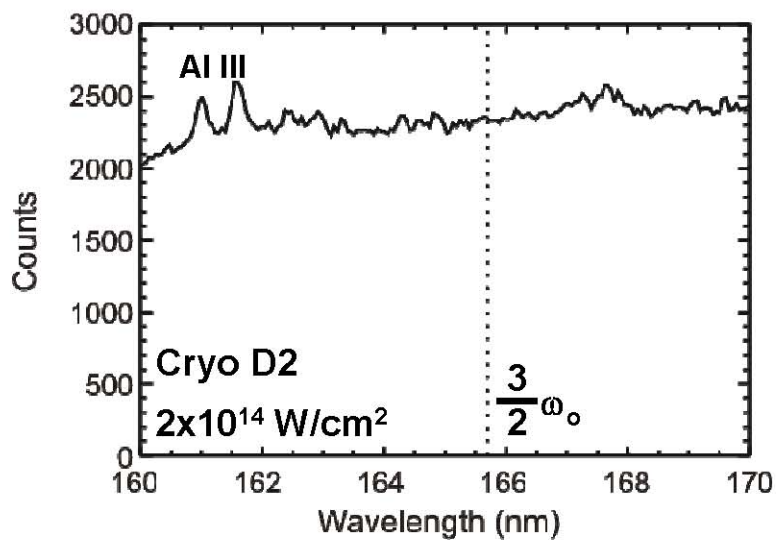
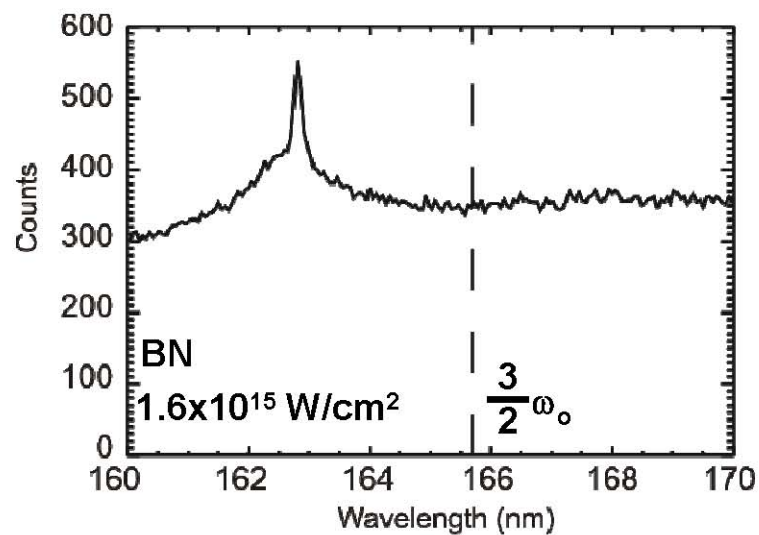
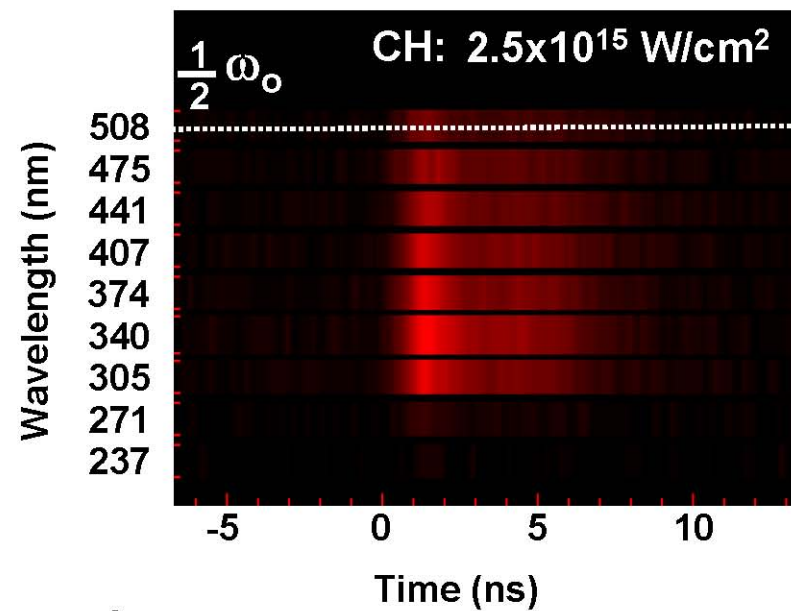


Fig. 10

a)



b)



c)

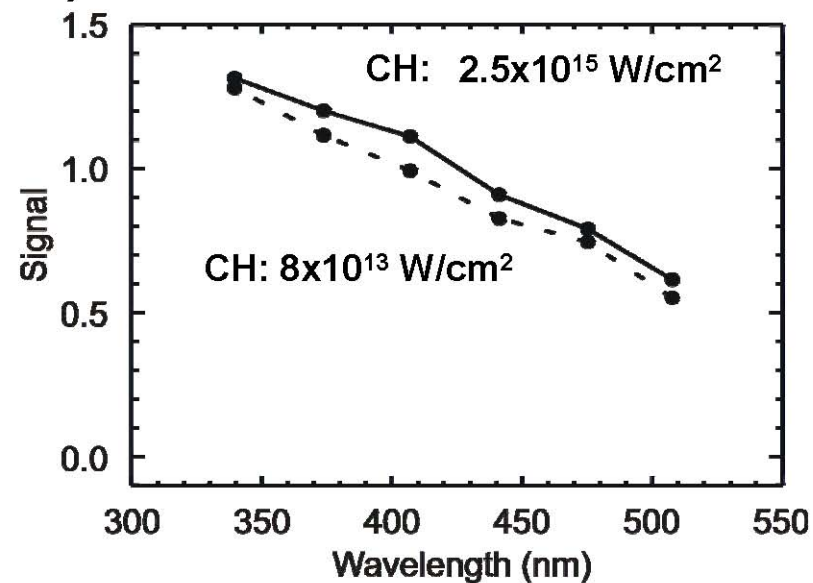


Fig. 11

Spike: $6 \times 10^{14} \text{ W/cm}^2$

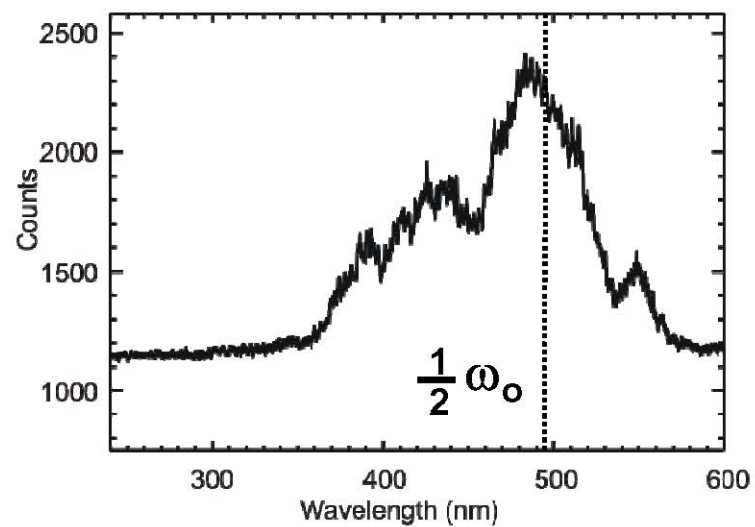
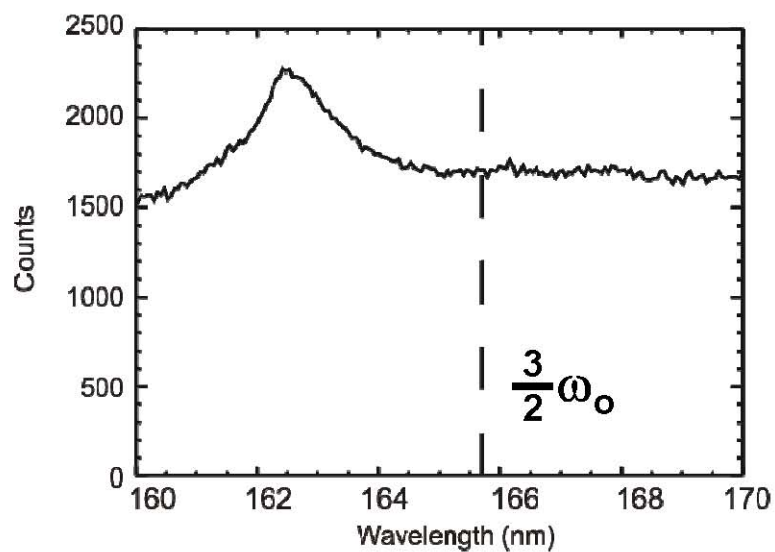
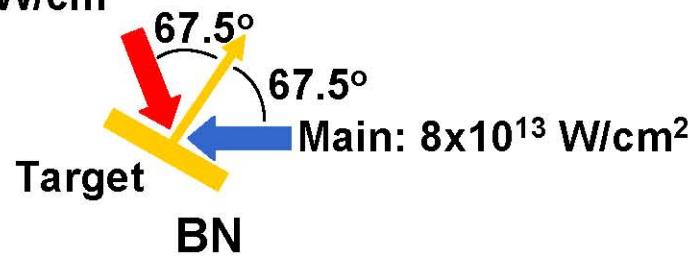


Fig. 12